High-Purity Copper Structures from a Perfluorinated Copper Carboxylate using Focused Electron Beam Induced Deposition and Post-Purification

Luisa Berger[1], Jakub Jurczyk[1,2], Katarzyna Madajska[3], Thomas Edward James Edwards[1], Iwona Szymańska[3], Patrik Hoffmann[4], Ivo Utke[1]*

[1]Empa - Swiss Federal Laboratories for Materials Science and Technology, Laboratory for Mechanics of Materials and Nanostructures, Feuerwerkerstrasse 39, 3602 Thun, Switzerland

[2] Faculty of Physics and Applied Computer Science, AGH University of Science and Technology Krakow, Al. Mickiewicza 30, 30-059 Kraków, Poland

[3]Faculty of Chemistry, Nicolaus Copernicus University in Toruń, Gagarina 7, 87 100 Toruń, Poland

[4]Empa - Swiss Federal Laboratories for Materials Science and Technology, Laboratory for Advanced Materials Processing, Feuerwerkerstrasse 39, 3602 Thun, Switzerland

ABSTRACT The electron induced modification of volatile physisorbed metalorganic molecules is the key process in focused electron beam induced deposition (FEBID). In this work, the perfluorinated copper carboxylate $[Cu_2(\mu-O_2CC_2F_5)_4]$, $(Cu_2(pfp)_4)$, was implemented in FEBID as

it has the highest metal to carbon ratio Cu:C = 1:6 compared to other Cu-precursors used so far. FEBID was obtained within a small temperature window of 120 - 130 °C. Transmission electron microscopy verified the presence of metal(oxide) nanocrystals within a carbonaceous matrix. The chemical composition analysis revealed the loss of about 80% of ligand material during the electron induced dissociation. The copper nanocrystals oxidized within a few minutes in films < 80 nm upon exposure to ambient conditions, while they were protected by a carbon-fluorine containing matrix in thicker areas of the deposits. A two-step post-growth annealing procedure with subsequent oxidizing and reducing atmosphere was used to purify the deposits. Pure copper crystals were formed in this step.

1. Introduction Copper is known for its low electrical resistivity and being, due to its abundance, significantly cheaper than similarly well conducting metals such as gold, silver. It is therefore widely used in electric circuits and microelectronics.

Usually, copper nanostructures are obtained in a wet-chemical approach resulting in nanoparticles and nanowires [1]. These techniques however, are not necessarily suitable for patterning as it is required in circuits. For this case, two step patterning approaches using electron beam lithography (EBL) [2] and vapor deposition techniques such as chemical vapor deposition (CVD) or atomic layer deposition (ALD) [3] are chosen and require a subsequent lift-off process. However, these fabrication techniques are limited to 2-dimensional deposits and flat substrates or need prefabricated 3-dimensional structures.

Focused electron beam induced deposition (FEBID) represents a highly flexible direct-write method for the deposition of many different materials with a high spatial resolution [4–7]. By introducing volatile precursor molecules into the chamber of a scanning electron microscope (SEM), the focused electron beam is used to locally dissociate molecules that are physisorbed on

the substrate surface. In contrast to EBL, material can be deposited on any substrate that is conductive with no morphological constraints using FEBID. After the electron induced precursor molecule modification, the volatile precursor fragments are pumped out of the chamber while the non-volatile fragments can be observed as local deposits on the irradiated area. Thanks to the small beam diameters of modern microscopes the lateral resolution of FEBI deposits reaches the nanometer range [8–11]. FEBID has proven to become a very versatile technique for the direct-write deposition of a large variety of materials including alloys [12–14] and magnetic materials [15]. It furthermore finds application in many different fields such as industrial mask repair [16–18], sensors [19–23], scanning probe tips [24–27] or nanophotonics and nanoplasmonics [28–35].

A challenging goal is the deposition of pure metal nanostructures using metal-organic precursors. The direct deposition of metals from carbon containing precursors such as silver with purities up to 70 at.% [36–38] from a carboxylate or iron [39], cobalt [40] and CoFe [14] with purities 80-90 at.% each from carbonyls were reported in literature. Besides that, different approaches were reported for the purification of the as-deposited metal containing material from the carbonaceous matrix [41–49].

Copper FEBID was realized with several Cu(I) and Cu(II) precursors so far but did not exceed a metal content of 25 at.% yet [50–52]. All of the reported precursors were symmetrical or asymmetrical β-diketonates. In this work we present the use of copper(II) pentafluoropropionate, $[Cu_2(\mu-O_2CC_2F_5)_4$ $(Cu_2(pfp)_4)$ as a novel FEBID precursor which was shown to evaporate around 140-160 °C[53]. The fluorine renders this copper precursor complex more volatile than fluorine-free cupric propionate or the copper oxalate which was studied as a metal organic framework only[54–56]. The propionic acid reported in Bret et al.[57] is very similar to the perfluorinated propionic acid used as ligand here. The fluorine makes it more volatile (compared to CH_3CH_2COOH) due to the

high electronegativity of fluorine and the absence of hydrogen bonds but does not necessarily increase deposition rates as suggested by Bret et al[57].

2. Results and Discussion:

2.1 Shape and Internal Structure of $Cu_2(pfp)_4$ deposits In comparison to a typical FEBID experiment which is conducted at room temperature, the following experiments were carried out at elevated process temperatures. $Cu_2(pfp)_4$ is a low volatility precursor for which the suitable deposition temperature window had to be determined. For all shown depositions, the gas injection system (GIS) was heated to 140°C and the substrate temperature was set to 130°C, leaving very little scope of variation. On the one hand, when lowering the substrate temperature by only 10°C, precursor condensation occurred on the substrate. On the other hand, when the substrate was heated to > 130°C no deposition was observed, presumably due to increased desorption rates, i.e. insufficiently long residence times of the molecules.
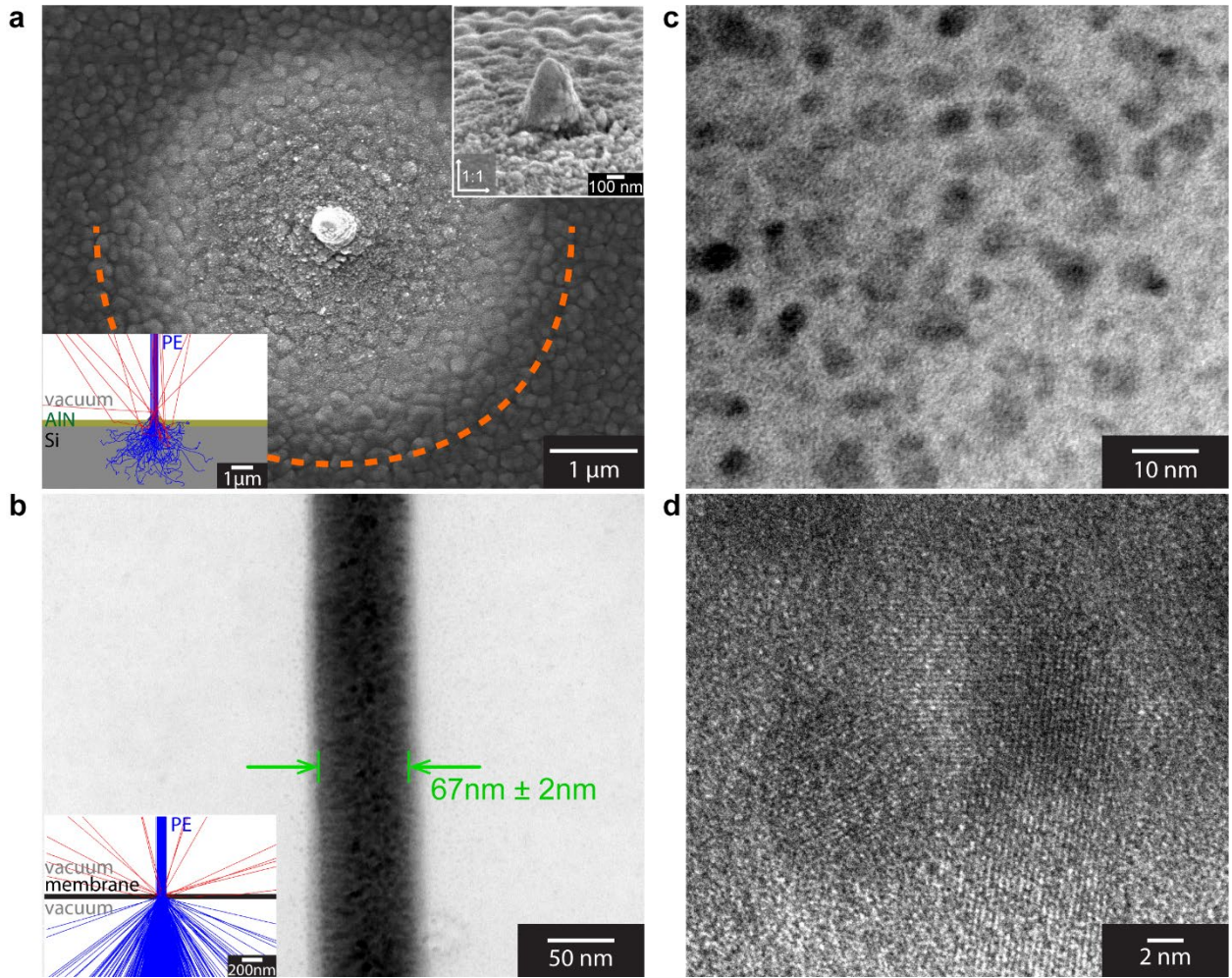
Figure 1 (a) SEM micrograph of a 20 keV, 460 pA dot deposit from $Cu_2(pfp)_4$ on an AlN/Si substrate (rough morphology). The halo extends to the theoretical backscattered electron range marked in orange (Kanaya-Okayama [58]). The upper right inset shows the central region in a 70° tilt view, 3-dimensional growth is observed here. The lower left inset displays the MC-simulated electron trajectories within the bulk substrate. (b) BF-STEM image of a 25 keV and 1.35 nA FEBID line deposited from $Cu_2(pfp)_4$ on a 50 nm thick SiN_x membrane. The inset shows the MC-simulated electron trajectories when interacting with the membrane. Note the avoidance of the halo deposit. (c) BF-STEM image showing metal(oxide) crystallites within the FEBID deposit on the membrane. (d) HR-TEM image of two individual metal(oxide) grains on the membrane with distinct lattice planes.

Figure 1a shows a dot deposited by irradiating the same point for 30 min with 20 keV acceleration voltage and a beam current of 0.46 nA (measured in a Faraday cup). The deposit can be described in two sections: the bright central area and a less pronounced halo area. The central part is thicker as can be seen in the inset where the central region is imaged with a 70° tilt view. The onset of 3-dimensional growth is visible and resulted in a tip of approximately 400 nm height. Of note is that the deposition rate in our experiment (about 0.1 μm^3 per nanoampere and 30 minutes) was very small. This is due to the very small residence time (high desorption rate) of adsorbates at these elevated temperatures. The deposition was conducted in the desorption driven regime[59] where the adsorbates desorb before being dissociated by the electrons. At a higher electron flux provided by the field emission gun the growth rate was observed to be about 10 times larger on the silicon nitride membrane. The halo region contains individual bright contrast grains that can be clearly distinguished from the substrate. This halo deposit is formed by secondary electrons (SE) that are generated when backscattered electrons (BSE) are emitted from the substrate. The Monte Carlo (MC) simulation in the lower left inset illustrates the trajectories of 75 electrons (20 keV) when interacting with a CuCF-deposit on an AlN(300nm)/Si bulk substrate. The blue lines describe the primary electron (PE) beam that crosses the interface between vacuum and substrate as well as the BSEs scattered within an interaction volume which depends on the bulk density and PE energy. The red lines correspond to emitted BSEs. The orange dashed line in the SEM image at 2700 nm from the center represents the theoretical maximum exit radius of BSEs generated by a primary electron (PE) beam of 20 keV when interacting with a Si bulk substrate as calculated according to Kanaya and Okayama [58], disregarding the 300nm AlN layer on the Si substrate. MC simulations showed that the AlN layer did not change this radius significantly. When compared to the deposit, the visible halo region does not reach this value. For

the analogous silver precursor $[Ag_2(\mu\text{-}O_2CC_2F_5)_2]$ in our previous work[37], the halo deposit coincided with this radius., probably due to larger deposition rates. The rough surface appearance in the background arises from the AlN film on the Si substrate which was used as a diffusion barrier.
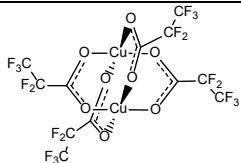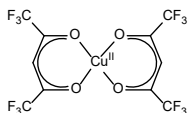
Figure 1b shows a bright field scanning transmission microscopy (BF-STEM) image of a line deposit on a 50 nm thick SiN_x membrane. The linewidth marked in the image was determined by measuring the intensity profiles and corresponds to the beam's spot size of FW(99.9%) = 69 nm (the full width comprising 99.9% of the electrons within the Gauss profile). As expected, the halo of this deposit is significantly smaller than of the one achieved on bulk substrates. This is due to the smaller interaction volume, which results in scattering ranges of several microns in bulk Si, but is mainly cut off in the membrane. Therefore, the BSE yield decreases 50 times (see Supporting Information) reducing the number of emitted electrons drastically. This is illustrated in the MC simulation of the trajectories of 10,000 electrons in the inset. The interaction of a 25keV beam (FW(99.9%) = 69 nm) with a 50 nm SiN_x membrane is simulated. Blue lines mark the trajectories of primary and transmitted electrons and emitted BSEs are displayed in red. The majority of electrons are transmitted without further scattering within the membrane and only a small number of electrons are backscattered. Therefore the main deposit lies within the FW(99.9%) of the impinging beam. The line width was determined to be 67 nm ± 2 nm which corresponds very well with the measured spot size of the electron beam.
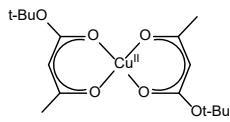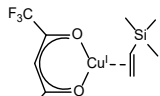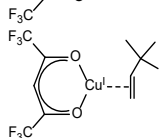
The higher magnification BF-STEM image (**Figure 1**c) shows grains with a mean diameter of 4.20 nm ± 0.95 nm dispersed in an amorphous matrix within the deposits. The high-resolution transmission electron micrograph (HR-TEM, **Figure 1**d) reveals the crystalline structure of those grains. Due to the small size of the deposited Cu particles, we assume that they are fully oxidized

after being exposed to air. The fast Fourier transformation (FFT) of the particles imaged in **Figure 1**d strongly suggest the presence of CuO and Cu_2O (see Supporting Information).

2.2 Deposit Composition Unlike the chelating β-diketonates, the $Cu_2(pfp)_4$ complex studied here consists of bridging carboxylates that bind over the oxygen to the copper atoms. It has a more favorable metal-to-carbon ratio (as well as ratios with other ligand elements), compared to previously used copper precursors (**Table 1**). Furthermore, the reduction of the initial copper to heteroatoms ratio Cu:(C,O,F) from 1:20 to 1:3.5 has to be highlighted here. They were obtained from energy dispersive X-ray spectroscopy (EDX) measurements (**Table 2**) described in this section. About 80% of the ligand material is removed upon electron irradiation. This is similar to $Cu(tbaoac)_2$ (86%) and (hfa)Cu(vtms) (84%) and is therefore amongst the best values reported so far. Additionally, we want to emphasize that in contrast to these two precursors, $Cu_2(pfp)_4$ is a hydrogen free precursor and deposits no oxygen. The details are described further down this section.

Table 1 – Copper precursors used for FEBID as reported in literature and the corresponding element ratios of the pristine molecule and the as deposited structures. As hydrogen is not detected by EDX it is omitted in the atomic ratio of as deposited FEBID material.

Precursor	Structure	pristine precursor Cu : C : O : F : H	as deposited (FEBID) Cu : C : O : F	Ref.
$Cu_2(pfp)_4$ [a]		1 : 6 : 4 : 10 : 0	1 : 1.5 : 0 : 2	this work
$Cu^{II}(hfa)_2$		1 : 10 : 4 : 12 : 2	1 : 6 : 2 : 0	[51,52,60,61]

Cu^{II}(tbaoac)$_2$		1 : 16 : 6 : - : 26	1 : 1 : 2 : -	[62]
(hfa)Cu^I(vtms)		1 : 10 : 2 : 6 : 13 (: 1 Si)	1 : 2 : 0.5 : 0 (: 0.5 Si)	[50–52]
(hfa)Cu^I(dmb)		1 : 11 : 2 : 6 : 13	1 : 3 : 1 : 0	[51,52]

[a] Cu$_2^{II}$(pfp)$_4$ exists as a dimer, see structure.

As evident from **Figure 1**, dot deposition resulted in two areas: a central part in the PE beam region and a halo in the region of emitted BSEs. The chemical composition was analyzed in both regions separately. **Table 2** displays the background and thin film corrected results of the energy dispersive X-ray spectroscopy (EDX) quantification taken with 3 keV on dot deposits fabricated on 100 nm SiN$_x$/Si bulk substrates. Aside from oxygen, all elements have comparable values within the measurement uncertainty. Therefore it can be assumed that the molecule dissociation and the co-deposition of ligand material is similar for both regions. Carbon and fluorine are with ~30at.% and ~40at.% the main contaminants. They can be attributed to co-deposited ligands, embedded in the structures in form of fragmented CF$_3$-CF$_2$ chains.

Table 2 – Background and thin film corrected EDX quantification results of dot deposits (on SiN$_x$/Si bulk) measured in the central pillar and halo region and dot deposits during the purification process (on SiO$_2$/Si) measured in the center (c.f. Figure 3). All spectra were measured at 3 keV primary beam energy.

	average dot deposits			deposit purification		
element (at.%)	center	halo	as deposited	O$_2$ flow, 250°C, 4h	H$_2$/N$_2$ flow, 250°C, 15h center	crystal

Cu	23	19	12	30	26	95
C	32	31	59	17	51	5
O	2	14	7	44	23	0
F	44	36	22	8	0	0

We assign the difference in oxygen content to the post-experiment oxidation of copper during the 2 min when the vacuum was broken to transfer the sample from the deposition microscope to the analytical tool. Since the halo deposit is only about 10 – 80 nm thin, the copper is less protected from atmospheric oxygen as in comparison to the thicker central region, so that a copper oxide was formed. The Cu:O ratio in the halo regions indicates the formation of copper(II)oxide (CuO). Based on these findings we propose the following simplified reaction pathways as illustrated in **Figure 2**.
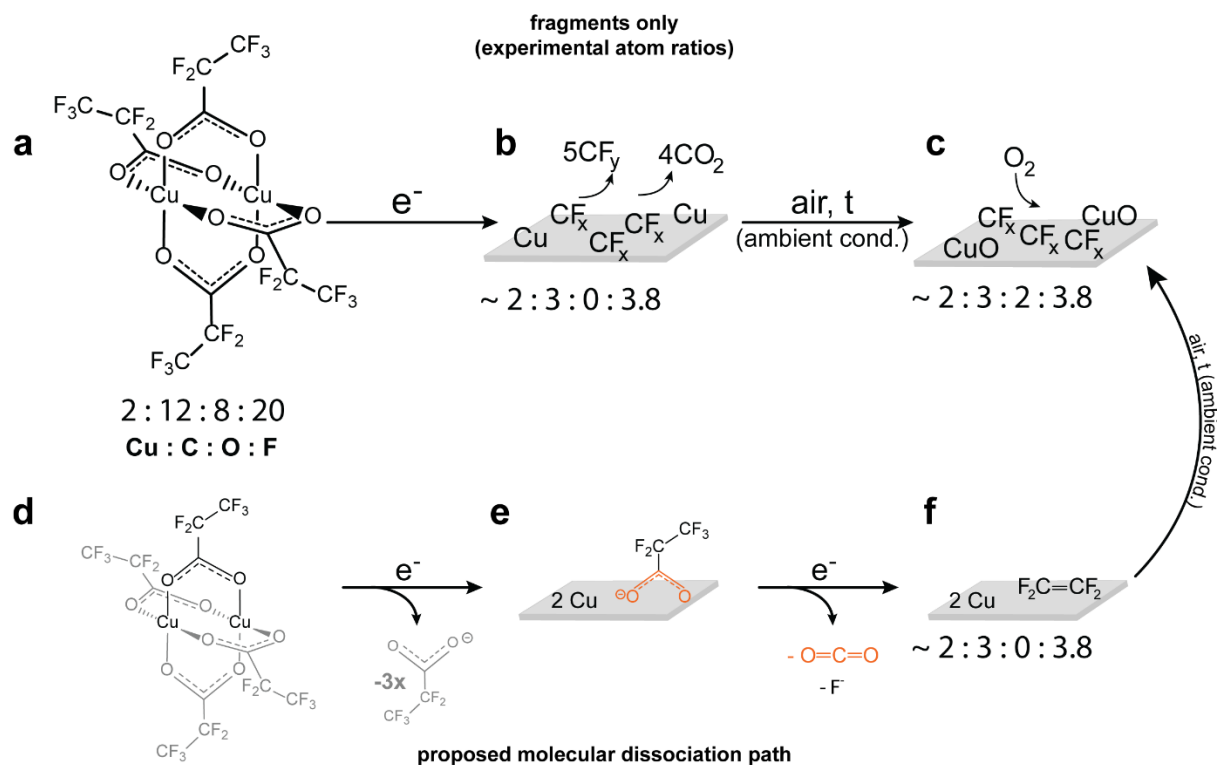
Figure 2 Proposed simplified electron induced dissociation path of the $Cu_2(pfp)_4$ precursor and the subsequent deposit oxidation in atmosphere. (a-c) Representation of deposited and desorbed fragments is based on the measured ratio of elements listed underneath. (d-f) Proposed molecular dissociation path based on gas phase mass spectrometric results from Lacko et al. [53]

The pristine precursor exists as a dimer as reported by Lacko et al.[53] The depicted dissociation pathway in Figure 3 leads to a thick deposit in the beam center or a thin halo deposit induced by BSEs. The number of deposited and desorbed fragments is estimated from the element ratios listed below the scheme. They are based on the EDX measurements of **Table 2**.

Initially, copper crystals within a matrix are probably formed (cf. **Figure 1**c and d). They are depicted as "*Cu*". According to the elemental ratios the matrix could be described with an average sum formula of C_3F_4 after electron induced dissociation, but the exact configuration is not known

to us, therefore they are described in **Figure 2**a-c as "CF_x" ($0 \leq x \leq 3$) for simplification. Following

the same approach, the average desorbing species has the sum formula $C_9F_{16}O_4$. Highly simplified,

the desorbing fragments are described as "CO_2" and "CF_y" ($2 \leq y \leq 3$). Interestingly, the element

ratios fit very well the molecular dissociation pathways described by Lacko et al. as presented in

Figure 3d-f (adapted from Ref.[53]). In agreement with their reported gas-phase cross-beam study

we can suggest the removal of three full ligands and the dissociation of the remaining pfp ligand

into CO_2, fluorine and the deposition of pure copper and $F_2C=CF_2$. The additional carbon atom in

the deposit (Figure 3b.2) may probably originate from carbon co-deposition from residual gases

in the deposition chamber. The exact molecular matrix compounds of our deposits cannot be

determined with EDX. Removal of CO_2 by electron induced desorption was also shown for other

Cu^{II} complexes and salts[54,55]. This explains the absence of oxygen in the original deposit.

Furthermore, the polarization by the electronegative CF_3-CF_2 chain facilitates the cleavage of the

ligand at the -COO^- carboxyl group forming volatile CO_2 which desorbs readily from the substrate.

The second reaction step depicts the oxidation of copper forming CuO (Figure 3c). This happens

when the vacuum is broken after deposition. Since the copper crystals are very small, as shown by

TEM measurements, they oxidize rapidly in the thin halo deposit. The high electron density in the

center leads to more deposition and therefore a higher amount of non-oxidized copper protected

from atmosphere within this structure. Note that the oxidation is time dependent and even the thick

central deposit showed a Cu:O ratio of 1:1 in aged samples.

The electrical resistivity at room temperature of the as deposited structures was measured with

a 4-point probe set-up and gave a high resistivity of 406 +/- 19 Ωcm in comparison to bulk Cu

with $1.6*10^{-6}$ Ωcm. We attribute this high resistivity not only to the dispersion of small copper

nanoparticles within an insulating fluorinated carbon matrix but especially to the subsequent oxidation of these copper crystallites in ambient conditions.

Reported high-purity structures in the as deposited state are often achieved with the help of autocatalysis[5,39,40,63–65]. In our case we could not achieve such a mechanism. The co-deposited CF_x ligand material leaves no free metal surfaces for potential catalytic reactions. Ideally, an increase of the substrate temperature during deposition would lead to more efficient CF_x fragment desorption and eventually cleaner copper structures. However, as stated above, the desorption rate of the full precursor molecule increased significantly upon heating and no more deposition was observed. Therefore, post-growth deposit purification was explored.

2.3 Post-growth Purification The most pressing challenge in the FEBI deposition of this copper precursor is the deposit oxidation when exposing it to ambient conditions. Post-experiment oxidation can be treated *ex-situ* using known purification methods[41,49]. Carbonaceous material from co-deposited ligands can be removed by oxidation via annealing in O_2 atmosphere. However, since copper is a non-noble metal, this oxidation step will also form CuO and Cu_2O. Therefore, a second purification step has to be introduced. Subsequent annealing in a reducing gas mixture, leads to the formation of Cu^0. In this work, a reducing gas mixture of 2% H_2 / 98% N_2 was used to reduce copper oxide to elemental copper. This procedure proved to be successful and pure copper was obtained. Due to the high mobility of this metal the initial shape of deposits could not be maintained and formation of copper crystals and islands was observed, as depicted in **Figure 3**. The direct annealing in the reducing gas mixture does not lead to full purification, because the carbon matrix is not removed (see Supporting Information). This stands in contrast to the

purification process reported by Jurczyk et al., where the carbon content in ruthenium deposits was successfully reduced with forming gas only[49]. This might be due to the fact that perfluorocarbons are more stable at higher temperatures than their respective fluorine-free hydrocarbon compounds. In the reported process, all incorporated carbon in the ruthenium deposits originated from non-halogenated allyls.

In the as deposited state the dot center on the left shows the same appearance as in **Figure 1** and consists of a relatively smooth, uniform carbonaceous matrix. After annealing it at 250°C for 4h in pure oxygen, the structure appearance changes. Local EDX measurements proved the formation of copper oxide and the presence of residual carbon and fluorine (**Figure 3**, red spectrum). The detailed quantification results are listed in **Table 2**. Even though the formation of oxide should lead to a volume increase, the structure collapsed. Therefore we assume that the carbon-fluorine matrix was partly removed, as is visible from the quantification results. The carbon content dropped from 59 at.% in the as deposited to 17 at.% in the annealed state. Similar holds true for the fluorine content reducing to 8 at.%. The copper was oxidized resulting in an almost 1:1 ratio of Cu:O. Since this removal is a function of temperature and time, a longer annealing period or higher temperatures would probably be necessary for full carbon removal.

The second annealing step was performed at 250°C for 15h in the reducing gas mixture. Here, the deposit shape was altered drastically. The deposit developed large, facetted crystals. Local EDX measurements on these large particles (**Figure 3**c, green star and spectrum) confirm that they are made of pure copper (95 at.%, see **Table 2**). As visible from the blue spectrum, the dot center still contains some residual carbon and non-reduced CuO due to insufficient annealing temperatures or times. The fluorine was removed completely in this step. Interestingly, a ring of crystals formed around the dot center. When comparing it to theoretical BSE range (**Figure 3**,

orange dashed line) it becomes visible, that the thin halo agglomerated and diffused towards the outside, forming the ring of copper crystals at this exact radius. The local measurement in the center of the structure shows an increase in carbon content (51 at.%) and some non-reduced CuO (Cu: 26 and O: 23 at.%). Higher carbon contents in the center can be attributed to the migration of purified copper to the outside of the structure, agglomerating into larger crystals and resulting in a residual carbon matrix in the probed volume (**Figure 3**c, blue star). Some of the Cu signal might also originate from the large crystals on top of the structure.
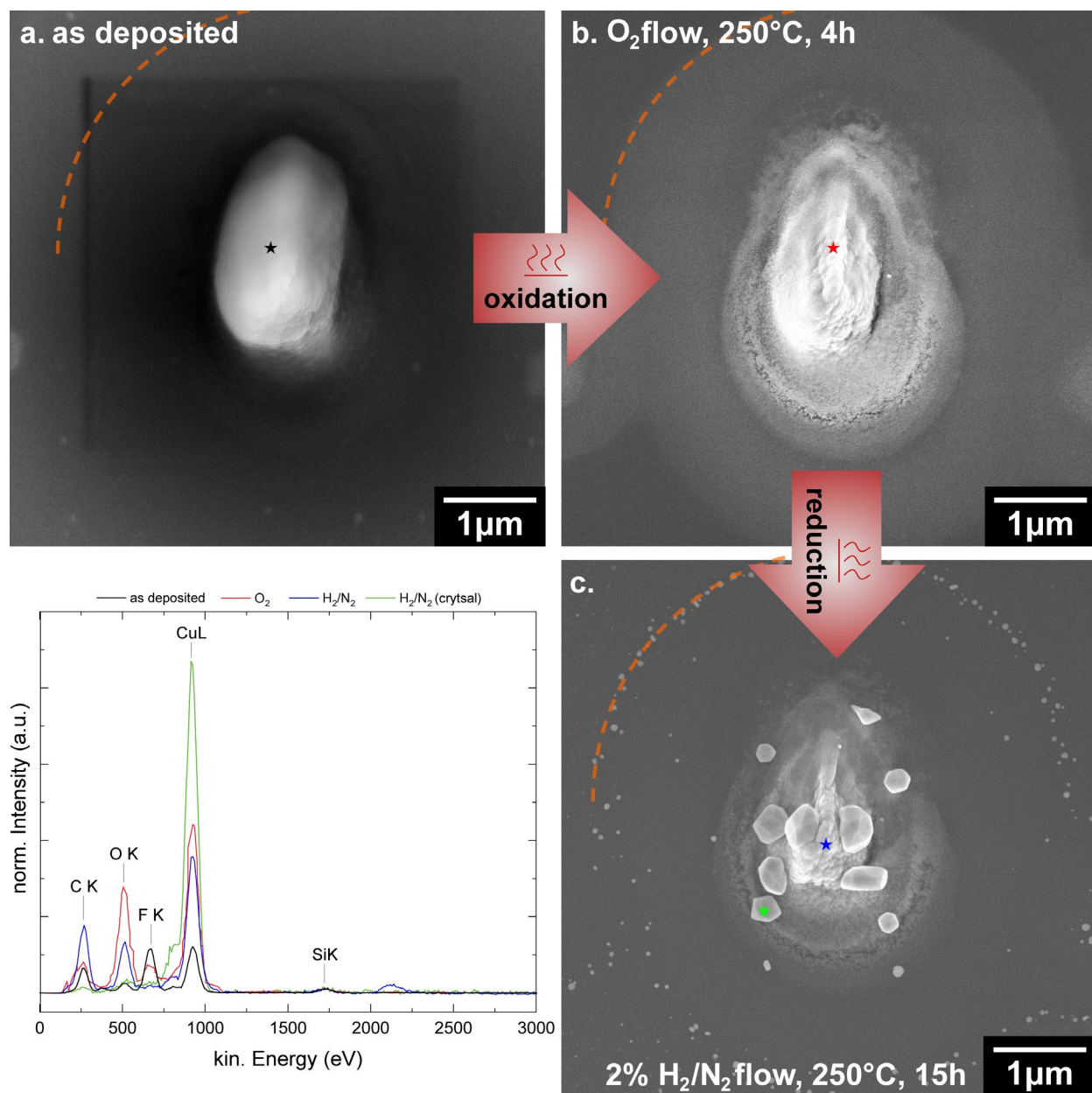
Figure 3 Spot deposit on SiO_2/Si. (a) as deposited with 20 keV for 60 min, relatively smooth and uniform center. A scanning window from previous observation is visible; (b) after annealing for 4h in O_2 flow at 250°C, the smooth matrix is partly removed; (c) after annealing for 15h in a reducing gas mixture, large facetted crystals appeared. The green star marks the point of local EDX measurement to prove the presence of pure copper (95 at.%). The orange dashed line marks the theoretical BSE range of this deposit. The graph shows the EDX spectra of deposits from $Cu_2(pfp)_4$

at the different processing steps. The intensity was normalized to the Si peak. Quantification is summarized in **Table 2**.

These observations demonstrate the difficulties that arise during the purification of copper FEBI deposits. Even though the material can be purified, the high mobility of copper prevents the preservation of the initially deposited shape and leads to agglomerations of large crystals.

3. Conclusions A perfluorinated copper carboxylate precursor, $Cu_2(pfp)_4$ $(Cu_2(\mu\text{-}O_2CC_2F_5)_4)$, was reported for the first time to be used in the local gas assisted focused electron beam induced deposition of copper. Long-term irradiation of a single spot resulted in the deposition of a 3-dimensional dot with a large halo. TEM investigations revealed the internal structure of those deposits to be nanocrystallites in the size range of around 4 nm embedded in an amorphous matrix.

Chemical composition studies showed that the electron induced dissociation resulted in the removal of large parts of the ligands, so that the ratio of copper to heteroatoms could be lowered from $1{:}20 \rightarrow 1{:}3.5$. This corresponds to the dissociation and desorption of about 80% of the ligand material during electron induced dissociation. The reported amorphous matrix consists of CF_x fragments which protect the initially deposited copper from oxidation in ambient conditions. However, very thin deposits as in the dot halo region were shown to oxidize immediately after exposure to air. The CF_x matrix and metal oxidation inhibited any possible self-catalytic dissociation of the precursor. Higher copper purity was therefore difficult to achieve in the as deposited state and a post-growth annealing process was implemented. The mobility of copper at elevated temperatures did not allow the preservation of the initially deposited shape, however, post-growth annealing in subsequent oxidizing and reducing atmosphere lead to the formation of pure copper.

Experimental Part

Precursor Synthesis The precursor $Cu_2(pfp)_4$ ($Cu_2(\mu\text{-}O_2CC_2F_5)_4$) was synthesized as reported by Szłyk and Szymańska [66].

FEBID Experiments Deposition was performed on native oxide Si substrates with a PVD-AlN layer (300 nm), a SiN_x (200nm) layer, or a thick SiO_2 (200nm) layer in a Hitachi S-3600 scanning electron microscope with a thermal emission tungsten filament using an electron energy of 20 keV and a beam current of 0.46 nA. The coatings provided a sufficiently thick diffusion barrier to avoid copper diffusion into silicon und thus non-reproducible results. No change in FEBID growth rate was detected for the different substrate types. For TEM analysis, deposits with a higher lateral resolution were fabricated on a SiN_x membrane (50nm thick) in a Philips XL-30 scanning electron microscope with a field emission gun (FEG). The electron energy was set to 25 keV with a beam current of 1.35 nA. The beam sizes were measured at full width at half maximum (FWHM) to be 170 ± 17 nm in the Hitachi S-3600 and 26.34 ± 0.43 nm in the Philips XL30 using the knife-edge method (see Supporting Information). The corresponding full widths comprising 99.9% of the electrons within the Gauss profile, FW(99.9%) were calculated to be 452 ± 34 nm (Hitachi) and 69 ± 1 nm (Philips). This corresponds to an average electron flux of $1.3*10^{19}$ $e^-/(cm^2*s)$ and $1.6*10^{21}$ $e^-/(cm^2*s)$, respectively. For all line and spot depositions the line scan and spot mode of the respective SEM software was used. The lines were scanned with 40 ms/line in the Philips XL30, corresponding to a dwell time of 635 μs/FW(99.9%) with FW(99.9%) = 69nm. Apart from the better lateral resolution the field emission gun also provided for a reasonable deposition rate on the SiN_x membrane.

The precursor was introduced into the microscope chamber through a homebuilt gas injection system (GIS). The GIS was designed to shorten molecule path lengths and is made of chemically inert stainless steel 1.445 with a final capillary of 0.38 mm inner diameter. The GIS was installed inside the chamber on a three-axis stage. The capillary opening was positioned at 300 μm lateral distance to the deposit and 200 μm above the substrate. For all depositions, the GIS was heated to 140 °C in order to provide the sufficient flux of the precursor molecules. The precursor flux was calculated to be $1.5*10^{15}$ molecules/(cm^2*s). The substrate temperature was set to 130 °C to avoid precursor condensation.

Morphology and Composition Analysis Deposits were analyzed using a Hitachi S-4800 system for high resolution scanning electron microscopy (HR-SEM). An EDAX silicon drift detector (SDD) was used for energy-dispersive X-ray spectroscopy (EDX). Spectra were recorded for 100 s at acceleration voltages of 3 and 16 keV, a beam current of 0.74 nA and a take-off angle of 38°. The detector background signal was subtracted and k-ratios determined with the EDAX TEAM™ software. The k-ratios were used in the thin-film analysis software SAMx STRATAGem to determine the elemental compositions of the deposits. Residual carbon and oxygen on the pristine substrate were taken into account by subtracting the measured quantities from the deposit quantification.

TEM Analysis The deposits on the SiN$_x$ membrane were imaged in a JEOL JEM 2200FS transmission electron microscope (TEM) operated at 200 kV in both high resolution imaging (HR-TEM) and bright field scanning (BF-STEM) modes.

Post-growth Purification Post-growth oxidation annealing was performed with pure oxygen (>99.999%, Carbagas) flowing through a tube furnace (Carbolite Ltd.) equipped with a dry pump. The temperature was set to 250°C and was heated with 20 K/min. Subsequent reduction was

performed in an MILA-5050 furnace (ADVANCE RIKO, Inc.) equipped with a rotary vane pump. The temperature was set to 250°C with a heating ramp of 20 K/min. Annealing was performed with a constant flow of a reducing gas mixture of H_2 and N_2 (2%/98%, Carbagas).

Simulations. Monte Carlo simulations of the electron distributions and trajectories were performed with the CASINO v3.3 software [67].

Graphics. Graphical data was further processed with Origin® 2018, Adobe Photoshop CC 2018, Adobe Illustrator CC 2018 and/or ChemDraw 2018.

Supporting Information The file contains an explanation of the beam diameter determination, backscattered electron yields and the FFT of Figure 1d. The following files are available

Supporting_Information.docx

Corresponding Author

*Ivo Utke, ivo.utke@empa.ch

Author Contributions

The manuscript was written through contributions of all authors. All authors have given approval to the final version of the manuscript.

References

(1)   Bhanushali, S.; Ghosh, P.; Ganesh, A.; Cheng, W. 1D Copper Nanostructures: Progress, Challenges and Opportunities. Small 2015, 11 (11), 1232–1252. https://doi.org/10.1002/smll.201402295.

(2)   Pease, R. F. W. Electron Beam Lithography. Contemp. Phys. 1981, 22 (3), 265–290. https://doi.org/10.1080/00107518108231531.

(3)   Gordon, P. G.; Kurek, A.; Barry, S. T. Trends in Copper Precursor Development for CVD and ALD Applications. ECS J. Solid State Sci. Technol. 2015, 4 (1), N3188–N3197.

(4)   Utke, I.; Hoffmann, P.; Melngailis, J. Gas-Assisted Focused Electron Beam and Ion Beam Processing and Fabrication. J. Vac. Sci. Technol. B Microelectron. Nanom. Struct. Process. Meas. Phenom. 2008, 26 (4), 1197–1276. https://doi.org/10.1116/1.2955728.

(5)   Utke, I.; Gölzhäuser, A. Small, Minimally Invasive, Direct: Electrons Induce Local Reactions of Adsorbed Functional Molecules on the Nanoscale. Angew. Chemie Int. Ed.

2010, 49 (49), 9328–9330. https://doi.org/10.1002/anie.201002677.

(6)   van Dorp, W. F.; Hagen, C. W. A Critical Literature Review of Focused Electron Beam Induced Deposition. J. Appl. Phys. 2008, 104 (8), 81301. https://doi.org/10.1063/1.2977587.

(7)   Huth, M.; Porrati, F.; Dobrovolskiy, O. V. Focused Electron Beam Induced Deposition Meets Materials Science. Microelectron. Eng. 2017, 185–186, 9–28. https://doi.org/https://doi.org/10.1016/j.mee.2017.10.012.

(8)   van Dorp, W. F.; van Someren, B.; Hagen, C. W.; Kruit, P.; Crozier, P. A. Approaching the Resolution Limit of Nanometer-Scale Electron Beam-Induced Deposition. Nano Lett. 2005, 5 (7), 1303–1307. https://doi.org/10.1021/nl050522i.

(9)   van Dorp, W. F.; Zhang, X.; Feringa, B. L.; Wagner, J. B.; Hansen, T. W.; De Hosson, J. T. M. Nanometer-Scale Lithography on Microscopically Clean Graphene. Nanotechnology 2011, 22 (50), 505303.

(10)   van Dorp, W. F.; Lazić, I.; Beyer, A.; Gölzhäuser, A.; Wagner, J. B.; Hansen, T. W.; Hagen, C. W. Ultrahigh Resolution Focused Electron Beam Induced Processing: The Effect of Substrate Thickness. Nanotechnology 2011, 22 (11), 115303.

(11)   van Dorp, W. F. Sub-10 Nm Writing: Focused Electron Beam-Induced Deposition in Perspective. Appl. Phys. A 2014, 117 (4), 1615–1622. https://doi.org/10.1007/s00339-014-8588-8.

(12)   Winhold, M.; Schwalb, C. H.; Porrati, F.; Sachser, R.; Frangakis, A. S.; Kämpken, B.; Terfort, A.; Auner, N.; Huth, M. Binary Pt–Si Nanostructures Prepared by Focused

Electron-Beam-Induced Deposition. ACS Nano 2011, 5 (12), 9675–9681. https://doi.org/10.1021/nn203134a.

(13) Shawrav, M. M.; Belić, D.; Gavagnin, M.; Wachter, S.; Schinnerl, M.; Wanzenboeck, H. D.; Bertagnolli, E. Electron Beam-Induced CVD of Nanoalloys for Nanoelectronics. Chem. Vap. Depos. 2014, 20 (7-8–9), 251–257. https://doi.org/10.1002/cvde.201407119.

(14) Porrati, F.; Pohlit, M.; Müller, J.; Barth, S.; Biegger, F.; Gspan, C.; Plank, H.; Huth, M. Direct Writing of CoFe Alloy Nanostructures by Focused Electron Beam Induced Deposition from a Heteronuclear Precursor. Nanotechnology 2015, 26 (47), 475701.

(15) De Teresa, J. M.; Fernández-Pacheco, A.; Córdoba, R.; Serrano-Ramón, L.; Sangiao, S.; Ibarra, M. R. Review of Magnetic Nanostructures Grown by Focused Electron Beam Induced Deposition (FEBID). J. Phys. D. Appl. Phys. 2016, 49 (24), 243003.

(16) Perentes, A.; Hoffmann, P. Focused Electron Beam Induced Deposition of Si-Based Materials From SiOxCy to Stoichiometric SiO2: Chemical Compositions, Chemical-Etch Rates, and Deep Ultraviolet Optical Transmissions. Chem. Vap. Depos. 2007, 13 (4), 176–184. https://doi.org/10.1002/cvde.200606583.

(17) Edinger, K.; Becht, H.; Bihr, J.; Boegli, V.; Budach, M.; Hofmann, T.; Koops, H. W. P.; Kuschnerus, P.; Oster, J.; Spies, P.; Weyrauch, B. Electron-Beam-Based Photomask Repair. J. Vac. Sci. Technol. B Microelectron. Nanom. Struct. Process. Meas. Phenom. 2004, 22 (6), 2902–2906. https://doi.org/10.1116/1.1808711.

(18) Edinger, K.; Wolff, K.; Steigerwald, H.; Auth, N.; Spies, P.; Oster, J.; Schneider, H.; Budach, M.; Hofmann, T.; Waiblinger, M. Bringing Mask Repair to the next Level. SPIE

Photomask Technol. 2014, 9235.

(19)   Friedli, V.; Santschi, C.; Michler, J.; Hoffmann, P.; Utke, I. Mass Sensor for in Situ Monitoring of Focused Ion and Electron Beam Induced Processes. Appl. Phys. Lett. 2007, 90 (5), 53106.

(20)   Schwalb, C. H.; Grimm, C.; Baranowski, M.; Sachser, R.; Porrati, F.; Reith, H.; Das, P.; Müller, J.; Völklein, F.; Kaya, A.; Huth, M. A Tunable Strain Sensor Using Nanogranular Metals. Sensors 2010, 10 (11), 9847–9856. https://doi.org/10.3390/s101109847.

(21)   Huth, M.; Kolb, F.; Plank, H. Dielectric Sensing by Charging Energy Modulation in a Nano-Granular Metal. Appl. Phys. A 2014, 117 (4), 1689–1696. https://doi.org/10.1007/s00339-014-8631-9.

(22)   Dukic, M.; Winhold, M.; Schwalb, C. H.; Adams, J. D.; Stavrov, V.; Huth, M.; Fantner, G. E. Direct-Write Nanoscale Printing of Nanogranular Tunnelling Strain Sensors for Sub-Micrometre Cantilevers. Nat. Commun. 2016, 7, 12487. https://doi.org/10.1038/ncomms12487 https://www.nature.com/articles/ncomms12487#supplementary-information.

(23)   Moczała, M.; Kwoka, K.; Piasecki, T.; Kunicki, P.; Sierakowski, A.; Gotszalk, T. Fabrication and Characterization of Micromechanical Bridges with Strain Sensors Deposited Using Focused Electron Beam Induced Technology. Microelectron. Eng. 2017, 176, 111–115. https://doi.org/https://doi.org/10.1016/j.mee.2017.03.009.

(24)   Utke, I.; Hoffmann, P.; Berger, R.; Scandella, L. High-Resolution Magnetic Co Supertips Grown by a Focused Electron Beam. Appl. Phys. Lett. 2002, 80 (25), 4792–4794.

https://doi.org/10.1063/1.1489097.

(25)   Lau, Y. M.; Chee, P. C.; Thong, J. T. L.; Ng, V. Properties and Applications of Cobalt-Based Material Produced by Electron-Beam-Induced Deposition. J. Vac. Sci. Technol. A 2002, 20 (4), 1295–1302. https://doi.org/10.1116/1.1481040.

(26)   Kindt, J. H.; Fantner, G. E.; Thompson, J. B.; Hansma, P. K. Automated Wafer-Scale Fabrication of Electron Beam Deposited Tips for Atomic Force Microscopes Using Pattern Recognition. Nanotechnology 2004, 15 (9), 1131–1134. https://doi.org/10.1088/0957-4484/15/9/005.

(27)   Belova, L. M.; Hellwig, O.; Dobisz, E.; Dan Dahlberg, E. Rapid Preparation of Electron Beam Induced Deposition Co Magnetic Force Microscopy Tips with 10 Nm Spatial Resolution. Rev. Sci. Instrum. 2012, 83 (9), 93711. https://doi.org/10.1063/1.4752225.

(28)   Koops, H. W. P.; Hoinkis, O. E.; Honsberg, M. E. W.; Schmidt, R.; Blum, R.; Böttger, G.; Kuligk, A.; Liguda, C.; Eich, M. Two-Dimensional Photonic Crystals Produced by Additive Nanolithography with Electron Beam-Induced Deposition Act as Filters in the Infrared. Microelectron. Eng. 2001, 57–58, 995–1001. https://doi.org/https://doi.org/10.1016/S0167-9317(01)00565-2.

(29)   Perentes, A.; Bachmann, A.; Leutenegger, M.; Utke, I.; Sandu, C.; Hoffmann, P. Focused Electron Beam Induced Deposition of a Periodic Transparent Nano-Optic Pattern. Microelectron.   Eng.   2004,   73–74,   412–416. https://doi.org/https://doi.org/10.1016/j.mee.2004.02.079.

(30)   De Angelis, F.; Das, G.; Candeloro, P.; Patrini, M.; Galli, M.; Bek, A.; Lazzarino, M.;

Maksymov, I.; Liberale, C.; Andreani, L. C.; Di Fabrizio, E. Nanoscale Chemical Mapping Using Three-Dimensional Adiabatic Compression of Surface Plasmon Polaritons. Nat. Nanotechnol. 2009, 5, 67. https://doi.org/10.1038/nnano.2009.348 https://www.nature.com/articles/nnano.2009.348#supplementary-information.

(31)   Höflich, K.; Yang, R. Bin; Berger, A.; Leuchs, G.; Christiansen, S. The Direct Writing of Plasmonic Gold Nanostructures by Electron-Beam-Induced Deposition. Adv. Mater. 2011, 23 (22-23), 2657–2661. https://doi.org/10.1002/adma.201004114.

(32)   Höflich, K.; Becker, M.; Leuchs, G.; Christiansen, S. Plasmonic Dimer Antennas for Surface Enhanced Raman Scattering. Nanotechnology 2012, 23 (18), 185303.

(33)   Winkler, R.; Schmidt, F.-P.; Haselmann, U.; Fowlkes, J. D.; Lewis, B. B.; Kothleitner, G.; Rack, P. D.; Plank, H. Direct-Write 3D Nanoprinting of Plasmonic Structures. ACS Appl. Mater. Interfaces 2017, 9 (9), 8233–8240. https://doi.org/10.1021/acsami.6b13062.

(34)   Woźniak, P.; De Leon, I.; Höflich, K.; Haverkamp, C.; Christiansen, S.; Leuchs, G.; Banzer, P. Chiroptical Response of a Single Plasmonic Nanohelix. Opt. Express 2018, 26 (15), 19275. https://doi.org/10.1364/oe.26.019275.

(35)   Höflich, K.; Feichtner, T.; Hansjürgen, E.; Haverkamp, C.; Kollmann, H.; Lienau, C.; Silies, M. Resonant Behavior of a Single Plasmonic Helix. Optica 2019, 6 (9), 1098. https://doi.org/10.1364/optica.6.001098.

(36)   Höflich, K.; Jurczyk, J.; Zhang, Y.; Puydinger dos Santos, M. V; Götz, M.; Guerra-Nuñez, C.; Best, J. P.; Kapusta, C.; Utke, I. Direct Electron Beam Writing of Silver-Based Nanostructures. ACS Appl. Mater. Interfaces 2017, 9 (28), 24071–24077.

https://doi.org/10.1021/acsami.7b04353.

(37) Berger, L.; Madajska, K.; Szymánska, I. B.; Polyakov, M. N.; Jurczyk, J.; Guerra-Nuñez, C.; Höflich, K.; Utke, I. Gas Assisted Silver Deposition with a Focused Electron Beam. Beilstein J. Nanotechnol. 2018, 9, 224–232. https://doi.org/doi:10.3762/bjnano.9.24.

(38) Höflich, K.; Jurczyk, J. M.; Madajska, K.; Götz, M.; Berger, L.; Guerra-Nuñez, C.; Haverkamp, C.; Szymanska, I.; Utke, I. Towards the Third Dimension in Direct Electron Beam Writing of Silver. Beilstein J. Nanotechnol. 2018, 9, 842–849. https://doi.org/doi:10.3762/bjnano.9.78.

(39) Lukasczyk, T.; Schirmer, M.; Steinrück, H.-P.; Marbach, H. Electron-Beam-Induced Deposition in Ultrahigh Vacuum: Lithographic Fabrication of Clean Iron Nanostructures. Small 2008, 4 (6), 841–846. https://doi.org/10.1002/smll.200701095.

(40) Fernández-Pacheco, A.; De Teresa, J. M.; Córdoba, R.; Ibarra, M. R. Magnetotransport Properties of High-Quality Cobalt Nanowires Grown by Focused-Electron-Beam-Induced Deposition. J. Phys. D. Appl. Phys. 2009, 42 (5), 55005.

(41) Langford, R. M.; Wang, T.-X.; Ozkaya, D. Reducing the Resistivity of Electron and Ion Beam Assisted Deposited Pt. Microelectron. Eng. 2007, 84, 784–788. https://doi.org/10.1016/J.MEE.2007.01.055.

(42) Geier, B.; Gspan, C.; Winkler, R.; Schmied, R.; D. Fowlkes, J.; Fitzek, H.; Rauch, S.; Rattenberger, J.; D. Rack, P.; Plank, H. Rapid and Highly Compact Purification for Focused Electron Beam Induced Deposits: A Low Temperature Approach Using Electron Stimulated H_2O Reactions. J. Phys. Chem. C 2014, 118 (25), 14009–14016.

https://doi.org/10.1021/jp503442b.

(43)   Stanford, M. G.; Lewis, B. B.; Noh, J. H.; Fowlkes, J. D.; Roberts, N. A.; Plank, H.; Rack, P. D. Purification of Nanoscale Electron-Beam-Induced Platinum Deposits via a Pulsed Laser-Induced Oxidation Reaction. ACS Appl. Mater. Interfaces 2014, 6 (23), 21256–21263. https://doi.org/10.1021/am506246z.

(44)   Plank, H.; Noh, J. H.; Fowlkes, J. D.; Lester, K.; Lewis, B. B.; Rack, P. D. Electron-Beam-Assisted Oxygen Purification at Low Temperatures for Electron-Beam-Induced Pt Deposits: Towards Pure and High-Fidelity Nanostructures. ACS Appl. Mater. Interfaces 2014, 6 (2), 1018–1024. https://doi.org/10.1021/am4045458.

(45)   Sachser, R.; Reizh, H.; Huzel, D.; Winhold, M.; Huth, M. Catalytic Purification of Directly Written Nanostructured Pt Microelectrodes. ACS Appl. Mater. Interfaces 2014, 6 (18), 15868–15874. https://doi.org/10.1021/am503407y.

(46)   Begun, E.; Dobrovolskiy, O. V.; Kompaniiets, M.; Sachser, R.; Gspan, C.; Plank, H.; Huth, M. Post-Growth Purification of Co Nanostructures Prepared by Focused Electron Beam Induced Deposition. Nanotechnology 2015, 26 (7). https://doi.org/10.1088/0957-4484/26/7/075301.

(47)   Shawrav, M. M.; Taus, P.; Wanzenboeck, H. D.; Schinnerl, M.; Stöger-Pollach, M.; Schwarz, S.; Steiger-Thirsfeld, A.; Bertagnolli, E. Highly Conductive and Pure Gold Nanostructures Grown by Electron Beam Induced Deposition. Sci. Rep. 2016, 6, 34003. https://doi.org/10.1038/srep34003
https://www.nature.com/articles/srep34003#supplementary-information.

(48)   Puydinger dos Santos, M. V; Szkudlarek, A.; Rydosz, A.; Guerra-Nuñez, C.; Béron, F.; Pirota, K. R.; Moshkalev, S.; Diniz, J. A.; Utke, I. Comparative Study of Post-Growth Annealing of Cu(Hfac)2, Co2(CO)8 and Me2Au(Acac) Metal Precursors Deposited by FEBID. Beilstein J. Nanotechnol. 2018, 9, 91–101. https://doi.org/doi:10.3762/bjnano.9.11.

(49)   Jurczyk, J.; Brewer, C. R.; Hawkins, O. M.; Polyakov, M. N.; Kapusta, C.; McElwee-White, L.; Utke, I. Focused Electron Beam-Induced Deposition and Post-Growth Purification Using the Heteroleptic Ru Complex (H3-C3H5)Ru(CO)3Br. ACS Appl. Mater. Interfaces 2019, 11 (31), 28164–28171. https://doi.org/10.1021/acsami.9b07634.

(50)   Utke, I.; Luisier, A.; Hoffmann, P.; Laub, D.; Buffat, P. A. Focused-Electron-Beam-Induced Deposition of Freestanding Three-Dimensional Nanostructures of Pure Coalesced Copper Crystals. Appl. Phys. Lett. 2002, 81 (17), 3245–3247. https://doi.org/10.1063/1.1517180.

(51)   Luisier, A.; Utke, I.; Bret, T.; Cicoira, F.; Hauert, R.; Rhee, S. W.; Doppelt, P.; Hoffmann, P. Comparative Study of Cu Precursors for 3D Focused Electron Beam Induced Deposition. J. Electrochem. Soc. 2004, 151 (8), C535–C537.

(52)   Luisier, A.; Utke, I.; Bret, T.; Cicoira, F.; Hauert, R.; Rhee, S.-W.; Doppelt, P.; Hoffmann, P. Comparative Study of Cu-Precursors for 3D Focused Electron Beam Induced Deposition. J. Electrochem. Soc. 2004, 151 (9), C590–C593. https://doi.org/10.1149/1.1779335.

(53)   Lacko, M.; Papp, P.; Szymańska, I. B.; Szłyk, E.; Matejčík, Š. Electron Interaction with Copper(II) Carboxylate Compounds. Beilstein J. Nanotechnol. 2018, 9, 384–398. https://doi.org/10.3762/bjnano.9.38.

(54)   Rückriem, K.; Grotheer, S.; Vieker, H.; Penner, P.; Beyer, A.; Gölzhäuser, A.; Swiderek, P.

Efficient Electron-Induced Removal of Oxalate Ions and Formation of Copper Nanoparticles from Copper(II) Oxalate Precursor Layers. Beilstein J. Nanotechnol. 2016, 7 (1), 852–861. https://doi.org/10.3762/bjnano.7.77.

(55)   Ahlenhoff, K.; Preischl, C.; Swiderek, P.; Marbach, H. Electron Beam-Induced Surface Activation of Metal-Organic Framework HKUST-1: Unraveling the Underlying Chemistry. J. Phys. Chem. C 2018, 122 (46), 26658–26670. https://doi.org/10.1021/acs.jpcc.8b06226.

(56)   Ahlenhoff, K.; Koch, S.; Emmrich, D.; Dalpke, R.; Gölzhäuser, A.; Swiderek, P. Electron-Induced Chemistry of Surface-Grown Coordination Polymers with Different Linker Anions. Phys. Chem. Chem. Phys. 2019, 21 (5), 2351–2364. https://doi.org/10.1039/c8cp07028h.

(57)   Bret, T.; Mauron, S.; Utke, I.; Hoffmann, P. Characterization of Focused Electron Beam Induced Carbon Deposits from Organic Precursors. Microelectron. Eng. 2005, 78–79, 300–306. https://doi.org/10.1016/J.MEE.2005.01.006.

(58)   Kanaya, K.; Okayama, S. Penetration and Energy-Loss Theory of Electrons in Solid Targets. J. Phys. D. Appl. Phys. 1972, 5 (1), 43.

(59)   Sanz-Hernández, D.; Fernández-Pacheco, A. Modelling Focused Electron Beam Induced Deposition beyond Langmuir Adsorption. Beilstein J. Nanotechnol. 2017, 8 (1), 2151–2161. https://doi.org/10.3762/bjnano.8.214.

(60)   Weber, M.; Koops, H. W. P.; Rudolph, M.; Kretz, J.; Schmidt, G. New Compound Quantum Dot Materials Produced by Electron-beam Induced Deposition. J. Vac. Sci. Technol. B Microelectron. Nanom. Struct. Process. Meas. Phenom. 1995, 13 (3), 1364–1368.

https://doi.org/10.1116/1.587854.

(61) Szkudlarek, A.; Vaz, A. R.; Zhang, Y.; Rudkowski, A.; Kapusta, C.; Erni, R.; Moshkalev, S.; Utke, I. Formation of Pure Cu Nanocrystals upon Post-Growth Annealing of Cu–C Material Obtained from Focused Electron Beam Induced Deposition: Comparison of Different Methods. Beilstein J. Nanotechnol. 2015, 6 (1), 1508–1517.

(62) Haverkamp, C.; Sarau, G.; Polyakov, M. N.; Utke, I.; dos Santos, M. V. P.; Christiansen, S.; Höflich, K. A Novel Copper Precursor for Electron Beam Induced Deposition. Beilstein J. Nanotechnol. 2018, 9, 1220.

(63) Vollnhals, F.; Drost, M.; Tu, F.; Carrasco, E.; Späth, A.; Fink, R. H.; Steinrück, H. P.; Marbach, H. Electron-Beam Induced Deposition and Autocatalytic Decomposition of Co(CO)3NO. Beilstein J. Nanotechnol. 2014, 5 (1), 1175–1185. https://doi.org/10.3762/bjnano.5.129.

(64) Utke, I.; Michler, J.; Gasser, P.; Santschi, C.; Laub, D.; Canton, M.; Buffat, P. A.; Jiao, C.; Hoffmann, P. Cross Section Investigations of Compositions and Sub-Structures of Tips Obtained by Focused Electron Beam Induced Deposition. Adv. Eng. Mater. 2005, 7 (5), 323–331. https://doi.org/10.1002/adem.200500061.

(65) Utke, I.; Hoffmann, P.; Dwir, B.; Leifer, K.; Kapon, E.; Doppelt, P. Focused Electron Beam Induced Deposition of Gold. J. Vac. Sci. Technol. B Microelectron. Nanom. Struct. 2000, 18 (6), 3168–3171. https://doi.org/10.1116/1.1319690.

(66) Szłyk, E.; Szymańska, I. Studies of New Volatile Copper(I) Complexes with Triphenylphosphite and Perfluorinated Carboxylates. Polyhedron 1999, 18 (22), 2941–

2948. https://doi.org/10.1016/S0277-5387(99)00199-0.

(67)   Demers, H.; Poirier-Demers, N.; Couture, A. R.; Joly, D.; Guilmain, M.; de Jonge, N.; Drouin, D. Three-Dimensional Electron Microscopy Simulation with the CASINO Monte Carlo Software. Scanning 2011, 33 (3), 135–146. https://doi.org/10.1002/sca.20262.

ABSTRACT GRAPHICS